AD-A262 204

CUMENTATION PAGE

Form Approved
OBM No. 0704-0188

(2)

2. Report Date.	3. Report Type and Dates Covered.
December 1992	Final - Journal Article

4. Title and Subtitle.
A Normal-Mode Analysis of Rapid Teleconnections in a Numerical Weather Prediction Model. Part I. Global Aspects

5. Funding Numbers.
Contract
Program Element No. 0601153N
Project No. RM35G84
Task No.
Accession No. DN659750
Work Unit No. 6.1-OMP

6. Author(s).
Ronald Gelaro

7. Performing Organization Name(s) and Address(es).
Naval Research Laboratory
Atmospheric Directorate
Monterey, CA 93943-5006

8. Performing Organization Report Number.
JA 432:056:90

9. Sponsoring/Monitoring Agency Name(s) and Address(es).
Office of Naval Research
Arlington, VA 22217

10. Sponsoring/Monitoring Agency Report Number.
JA 432:056:90

11. Supplementary Notes.
Published in Monthly Weather Review.

12a. Distribution/Availability Statement.
Approved for public release; distribution is unlimited.

12b. Distribution Code.

13. Abstract *(Maximum 200 words).*

Global-scale interactions between the tropics and extratropics are investigated using a version of the U.S. Navy's global operational numerical weather prediction model. The primary goals of this study are 1) to demonstrate the importance of atmospheric teleconnections for medium-range numerical weather prediction and 2) to analyze the evolution and dynamic structure of the response in a sophisticated numerical forecast model. The model normal modes are used as the principal diagnostic tool for analyzing the response to sea surface temperature anomalies in the tropical Pacific. By monitoring the energy growth in the dominant horizontal and vertical modes and comparing these with conventional difference-field diagnostics, it is shown that the character of the long-term response is well established within one to two weeks after the heating anomaly is introduced. The growth rates and structures of these modes provide insights into the dynamic processes that control the model response. In the tropics, enhanced convection is clearly the dominant forcing mechanism for these models. In the extratropics, a more complicated picture arises in which both meridionally propagating energy and in situ instabilities in the ambient flow appear to be important mechanisms for producing the observed wave patterns. The results clearly demonstrate that tropical forcing can have a significant global impact on time scales relevant to medium-range numerical weather prediction.

93 2 00 [illegible]

93-05945

15pp

14. Subject Terms.
Planetary boundary layer, ocean mixed layer, air-sea interaction

16. Price Code.

17. Security Classification of Report.	18. Security Classification of This Page.	19. Security Classification of Abstract.	20. Limitation of Abstract.
Unclassified	Unclassified	Unclassified	SAR

Reprinted from MONTHLY WEATHER REVIEW, Vol. 120, No. 12, December 1992
American Meteorological Society

A Normal-Mode Analysis of Rapid Teleconnections in a Numerical Weather Prediction Model. Part I: Global Aspects

RONALD GELARO

Naval Research Laboratory, Monterey, California

(Manuscript received 5 June 1991, in final form 2 March 1992)

ABSTRACT

Global-scale interactions between the tropics and extratropics are investigated using a version of the U.S. Navy's global operational numerical weather prediction model. The primary goals of this study are 1) to demonstrate the importance of atmospheric teleconnections for medium-range numerical weather prediction and 2) to analyze the evolution and dynamic structure of the response in a sophisticated numerical forecast model. The model normal modes are used as the principal diagnostic tool for analyzing the response to sea surface temperature anomalies in the tropical Pacific. By monitoring the energy growth in the dominant horizontal and vertical modes and comparing these with conventional difference-field diagnostics, it is shown that the character of the long-term response is well established within one to two weeks after the heating anomaly is introduced. The growth rates and structures of these modes provide insights into the dynamic processes that control the model response. In the tropics, enhanced convection is clearly the dominant forcing mechanism for these modes. In the extratropics, a more complicated picture arises in which both meridionally propagating energy and in situ instabilities in the ambient flow appear to be important mechanisms for producing the observed wave patterns. The results clearly demonstrate that tropical forcing can have a significant global impact on time scales relevant to medium-range numerical weather prediction.

In Part II of this study, the normal-mode diagnostic approach is extended by developing a technique for partitioning the modes according to their latitudinal variances in order to examine the tropical and extratropical responses in further detail. It is shown that the modes are a powerful and flexible tool for diagnosing the behavior of a complicated model.

1. Introduction

There is no doubt that tropical forcing can have a significant impact on the global circulation at midlatitudes (e.g., Bjerknes 1969; Horel and Wallace 1981; Wallace and Gutzler 1981; Webster 1981; Hoskins and Karoly 1981; Geisler et al. 1985; Pitcher et al. 1988). Such interactions between the tropics and extratropics, commonly referred to as *teleconnections*, are often associated with anomalous variations in tropical sea surface temperature (SST), such as those that occur in conjunction with the El Niño–Southern Oscillation (ENSO) phenomenon (Julian and Chervin 1978). There is now growing evidence, however, that, in addition to changes in the global-scale standing wave pattern, tropical forcing may have a crucial impact on the evolution of atmospheric phenomena on a wide range of spatial and temporal scales. For example, studies by Kok and Opsteegh (1985) and Mechoso et al. (1987) indicate that smaller-scale transient eddies may also be affected by tropical forcing anomalies. In addition, it has been shown by Tiedtke (1984) and by Donner et al. (1982) that the response of general circulation models (GCMs) may be quite sensitive to even minor variations in model-predicted diabatic forcing rates. These and other results suggest that interactions between the tropics and midlatitudes occur regularly and are an important component of the dynamics of the global circulation. Where numerical weather prediction (NWP) is concerned, these results suggest that certain systematic forecast errors at midlatitudes may in fact be linked directly to systematic errors in model-predicted tropical forcing.

At the present time, much of what is known about the structure and dynamics of tropical–midlatitude interactions has been learned from studies involving relatively simple models whose behavior can be easily interpreted. These studies have shown that perturbations in the tropical atmosphere caused by diabatic forcing are separable into two basic types of motions according to their vertical structures (Lim and Chang 1983). The first type tends to be trapped at low latitudes and is characterized by cellular motion in which the large-scale flow is of the opposite sign at upper and lower levels. The second type is characterized by large-scale flow that has the same sign at all levels and can propagate meridionally from the tropics to high latitudes. The latter may produce the global teleconnection patterns [e.g., the Pacific–North American (PNA) pat-

Corresponding author address: Dr. Ronald Gelaro, Naval Research Laboratory, Atmospheric Directorate, Monterey, CA 93943-5006.

tern, Horel and Wallace 1981; Wallace and Gutzler 1981] often associated with the atmospheric response to tropical SST anomalies.

While idealized models have successfully reproduced certain qualitative aspects of the observed response, much remains unknown about the dynamics of this response in the atmosphere, which may be complicated by processes such as waveguiding by subtropical jets and instabilities in the ambient flow. Although there now exists a considerable amount of data documenting the response of sophisticated GCMs to anomalous tropical forcing (e.g., Keshavamurty 1982; Blackmon et al. 1983; Shukla and Wallace 1983; Palmer and Mansfield 1986; Mechoso et al. 1987; Pitcher et al. 1988), little has been presented about the details of the modal structure and the dynamics of the response in these models or about the extent to which these characteristics agree with results from idealized modeling studies. In addition, most of these studies have examined the long-term (seasonal to interannual) impact of tropical forcing, focusing little attention on time scales relevant to NWP.

In this study, the normal modes of a sophisticated NWP model are utilized to investigate tropical–midlatitude interactions. The experimental approach is to analyze the model response to imposed SST anomalies in the tropical Pacific. The main objectives are

1) to examine the medium-range global impact of tropical forcing;
2) to investigate the evolution and dynamic structure of this response in a realistic system.

A secondary objective is to demonstrate how the normal modes may be used effectively to diagnose the behavior of complicated models. These objectives differ from those of many previous GCM studies of atmospheric teleconnections, which have provided more of a climatological overview of how the atmosphere responds to tropical heating anomalies.

The model used in this study is a version of the forecast component of the Navy Operational Global Atmospheric Prediction System (NOGAPS), described by Hogan and Rosmond (1991). The results are reported in two parts, this paper being the first part. The analysis in this paper is conducted from a global perspective, allowing exploitation of the simple form of the normal-mode energy equations. In the following section, the model and its normal modes are briefly described. In section 3, we describe the numerical experiments that provide the data for this study. In section 4, the time-averaged model response is examined using conventional difference-field diagnostics. This provides a basis for comparison with previous studies. In section 5, we begin the normal-mode analysis of the global response. The evolution of the response is analyzed in terms of the energy of the modes. In section 6, the dominant horizontal structures of the response are identified and their evolution is examined. Finally, in section 7, some conclusions and speculations based on this work are presented.

In Part II (Gelaro 1992; hereafter referred to as GII), we extend the analysis in this paper by investigating the tropical and extratropical components of the response in detail. A new technique is developed whereby the normal modes are partitioned according to their latitudinal variances, allowing us to analyze the evolution and structure of the response in each region and to make inferences about the dynamic mechanisms that produce them.

2. Description of the model and normal modes

The model used in this study is version 3.0 of NOGAPS, which served as the U.S. Navy's operational global NWP model between January 1988 and March 1989. NOGAPS is a complete real-time forecast system consisting of an optimal-interpolation (OI) analysis scheme (Barker et al. 1989), a nonlinear normal-mode initialization (NNMI) scheme, and a global forecast model (Hogan et al. 1991). The forecast model is spectral in both horizontal dimensions, with a triangular truncation at wavenumber 47 (T47 truncation), which corresponds to a transform grid with 144 equally spaced longitudinal points and 72 Gaussian latitudes (roughly, 2.5° horizontal resolution). It has 18 vertical levels defined in terms of σ coordinates. The time-integration scheme is a centered semi-implicit scheme (Kwizak and Robert 1971) with a Robert (1966) time filter. A biharmonic (∇^4) spatial filter is employed to smooth extremely small-scale features.

NOGAPS contains an extensive array of parame-

TABLE 1. Values of $\bar{T}_l$ calculated from a model control run, and the corresponding set of equivalent depths h_l. Note that l is used as a model-level index for σ and $\bar{T}$, but refers to the ordering of the vertical modes in the case of h.

l	σ	$\bar{T}_l$ (K)	h_l (m)
1	0.008	229.25	9669.53
2	0.028	209.14	3224.16
3	0.049	198.15	801.71
4	0.092	199.12	308.66
5	0.136	214.05	130.55
6	0.187	217.82	63.85
7	0.247	227.33	40.60
8	0.315	236.96	21.30
9	0.393	247.70	11.48
10	0.482	258.23	6.63
11	0.575	266.92	3.99
12	0.669	273.94	2.36
13	0.759	279.79	1.45
14	0.839	283.94	0.75
15	0.904	287.66	0.40
16	0.950	290.40	0.18
17	0.978	291.83	0.10
18	0.995	292.08	0.02

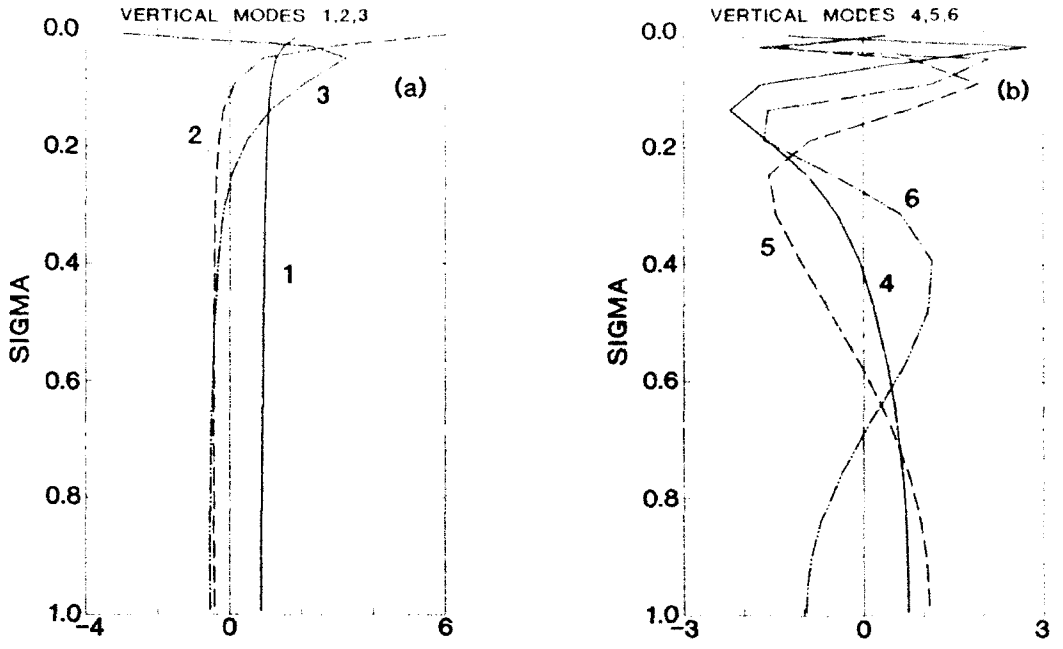

FIG. 1. The first six vertical modes of the 18-level NOGAPS model, based on the parameter values in Table 1 (signs are arbitrary).

terized physical processes, including those for gravity-wave drag, vertical fluxes of moisture, heat and momentum, cumulus convection, large-scale precipitation, shallow cumulus mixing, and radiation. Of particular note are the cumulus convection scheme, which is a modified version of the Arakawa–Schubert (A–S) scheme (Arakawa and Schubert 1974; Lord et al. 1982), and the vertical flux calculations, which are based on the K-theory formulation of Louis (1979). Ground temperature is predicted over land, while SST remains fixed at its initial values. The latter are obtained from daily analyses produced by Fleet Numerical Oceanography Center (FNOC).

The normal modes describe the spectrally truncated mass and momentum fields and are derived from the adiabatic model equations linearized about a basic state at rest with a horizontally uniform surface pressure field $\bar{p}_s$ and a horizontally uniform, vertically varying, temperature field $\bar{T}(\sigma)$. The values of $\bar{p}_s$ and $\bar{T}(\sigma)$ used in this study are their respective global-mean values averaged over days 21–50 of a control simulation. There are 18 vertical modes (corresponding to the number of vertical levels) numbered $l = 1, \cdots, 18$, in which $l = 1$ denotes the gravest, or external mode. The calculated values of $\bar{T}(\sigma)$ (or $\bar{T}_l$) used in this study are listed in Table 1, while the vertical structures of the six gravest modes are shown in Fig. 1. The horizontal structures of the modes are obtained in a standard fashion based on the separability of the linearized system. Further details are given in Hogan et al. (1991).

3. Numerical experiments

The data for this study were obtained from two pairs of 50-day simulations, each consisting of a control run and an anomaly run. The two runs differed only in that a localized positive SST anomaly was added to the initial climatological SST values of the anomaly run. The SST anomaly used in these simulations was located in the western Pacific and is shown schematically in Fig. 2. It is equatorially symmetric, extending latitudinally from approximately 14°N to 14°S, and longitudinally from 105° to 170°E. The magnitude of

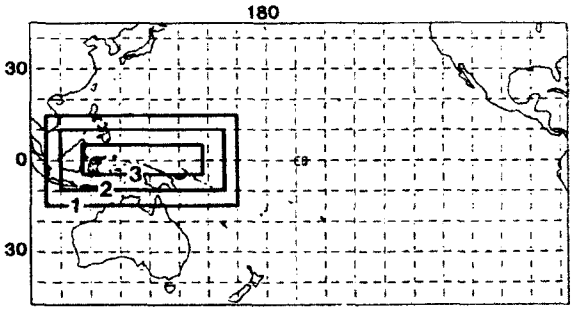

FIG. 2. Schematic representation of the positive temperature anomaly added to the climatological SST values in the anomaly run. The outermost contour encloses a region of 1°C anomalous warming, while the innermost contour encloses a region of 3°C anomalous warming.

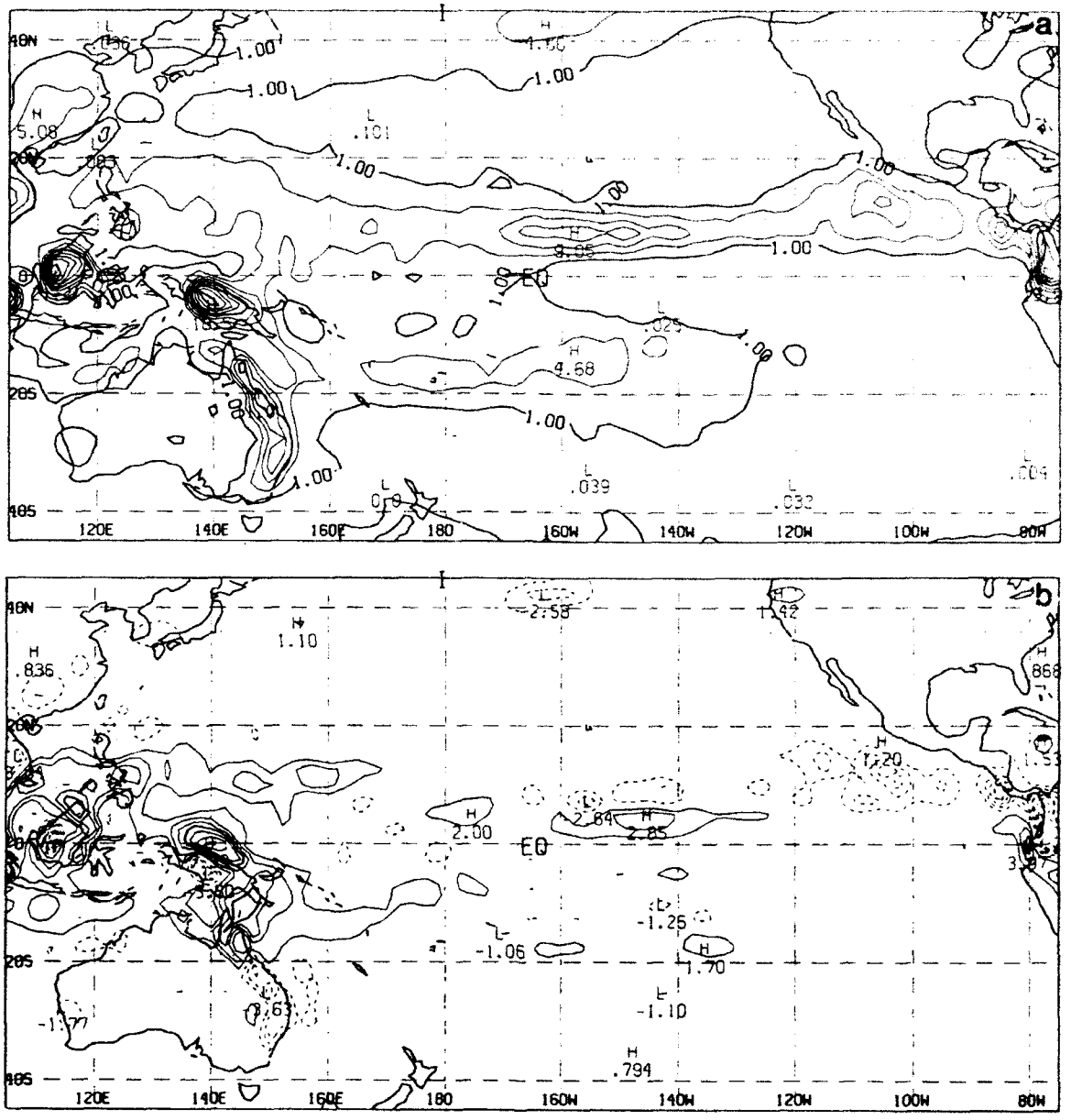

FIG. 3. The 30-day mean 12-h accumulated precipitation at 1200 UTC over the Pacific Ocean for days 21–50 of (a) the control run and (b) the response field. The minimum contour in (a) is 1 mm (12 h)$^{-1}$, with contours every 2 mm (12 h)$^{-1}$ thereafter. In (b) the contour interval is 1 mm (12 h)$^{-1}$, with negative values denoted by dashed lines.

the anomaly increases from +1°C at its outer boundary to +3°C at its center. This is substantially larger than observed SST anomalies in this region, but generally comparable with those used in other modeling studies cited in section 1. The inability of many GCMs to show significant responses to realistic SST anomalies remains a major shortcoming of these models, but is not of critical importance to the objectives of the present study.

The full SST anomaly was introduced at the beginning of the simulations and kept constant in time. Although there should be no significant changes in the seasonally averaged model response as to whether the anomaly is introduced gradually or abruptly some time

prior to the beginning of the averaging period (e.g., Mechoso et al. 1987), there may be some differences during the early stages of the simulations. In particular, there is evidence of a brief period of model shock but no abrupt changes in the rotational component of the flow. This is discussed further in section 5.

The initial conditions for the control run in the first pair of simulations were based on the NOGAPS analysis from 1200 UTC 15 December 1985, while those for the second pair were based on the NOGAPS analysis from 1200 UTC 13 December 1987. The model output was archived at 24-h intervals, so that the output data represent the instantaneous values of the fields at 1200 UTC on each day of the simulation. Composite control and anomaly datasets were formed by averaging the output for a given number of days from both the 1985 and 1987 Northern Hemisphere wintertime cases. The results that will be discussed in the following sections are based on these composite datasets.

4. Time-mean response

This section presents some of the general characteristics of the time-mean model response. We define the response as the difference δ between the control C and anomaly A simulations, so that, $\delta = A - C$. The time-mean response is then defined as the composite 30-day mean value of δ for days 21–50 of the simulations. The averaging was begun at day 21 in order to ensure that the model had reached an approximate equilibrium state. Evidence that the model response achieves equilibrium by day 20 is presented later.

Figures 3a and 3b shows the 30-day mean 12-h accumulated precipitation from 0000 to 1200 UTC over the Pacific Ocean for the control run and the response field, respectively. The precipitation pattern for the control run in Fig. 3a is rather typical for the tropical Pacific Ocean during the Northern Hemisphere winter. There is a well-defined intertropical convergence zone (ITCZ) centered near 5°–10°N that spans most of the Pacific Ocean, with maximum precipitation rates of 7–10 mm (12 h)$^{-1}$. The location and strength of this feature are reasonable for the middle of winter in the Northern Hemisphere. There are also locally larger maxima over the maritime continent and near the extreme west coast of South America. The precipitation rates in these regions are on the order of 15–20 mm (12 h)$^{-1}$.

The response field shown in Fig. 3b indicates that precipitation has been enhanced substantially in the central and western parts of the region of increased SST, especially over New Guinea and the extreme northeastern part of Australia. The maximum precipitation rates in this area range from 5 to 10 mm (12 h)$^{-1}$ and are comparable with those obtained by Keshavamurty (1982) and Blackmon et al. (1983) in GCM studies of SST anomalies in the central Pacific. These features, combined with the negative precipitation anomalies over the extreme eastern Pacific, are consistent with a more vigorous Walker circulation.

Figure 4 shows the area-averaged 30-day mean cumulus-heating profiles in the region of the SST anomaly. The increased SST results in an increase in cumulus heating of slightly more than 1 K day^{-1} in the middle and upper levels. The dramatic difference in the character of the profiles in the lowest levels is due primarily to increased precipitation and evaporative cooling in the anomaly run compared with an unrealistic overabundance of moisture at these levels in the control run.

Figure 5 shows the 30-day mean response of the velocity potential at 150 mb. The divergent component of the wind is directed perpendicular to the contours toward positive values. The results clearly indicate that there is increased upper-level horizontal divergence associated with the increased convection in the vicinity of the SST anomaly. This pattern, in turn, implies increased upward motion throughout the troposphere in this region, with convergence and downward motion over most of the Atlantic and Europe. This is consistent with the results in Figs. 3b and 4.

The enhanced Walker circulation is also evident in Fig. 6, which shows the 30-day mean vector wind response at 150 and 925 mb. In Fig. 6a, there are anomalous westerlies at 150 mb extending across most of

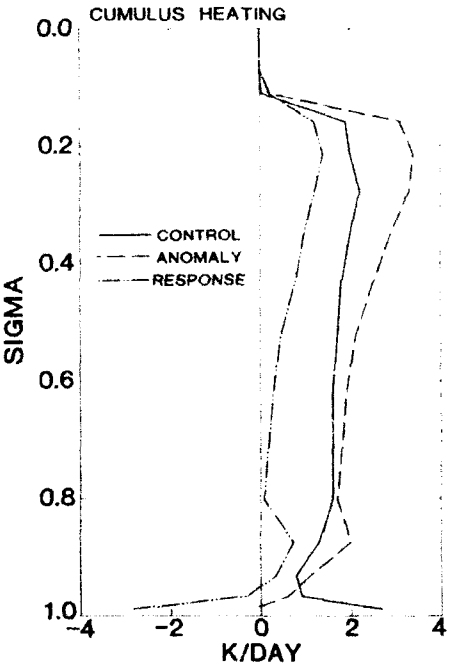

FIG. 4. Area-averaged 30-day mean cumulus-heating profiles over the region of increased SST.

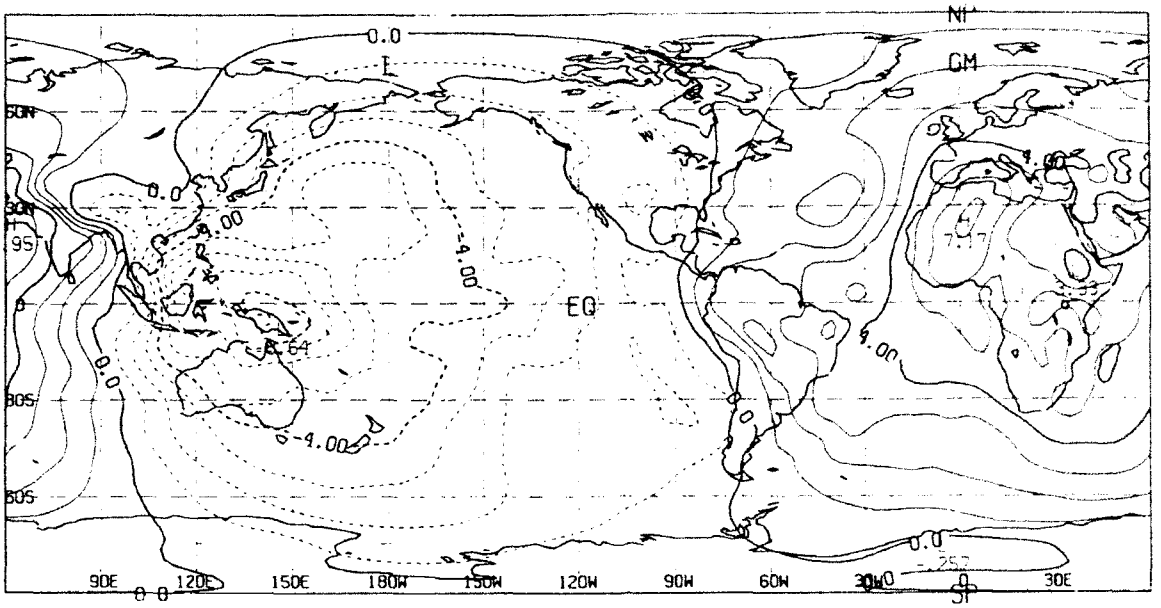

FIG. 5. The 30-day mean velocity-potential response at 150 mb. The divergent component of the wind is directed perpendicular to the contours from lower to higher values. The contour interval is 1.0×10^6 m^2 s^{-1}, with negative values denoted by dashed lines.

the equatorial Pacific, indicating flow away from the SST anomaly lying to the west. These anomalies are on the order of 10 m s^{-1}. To the west and north of New Guinea, there are easterlies of similar magnitude. Note the anticyclonic couplet on the poleward flanks of the SST anomaly. The situation is reversed at 925 mb, in Fig. 6b, where the flow is weakly convergent over New Guinea and there are easterlies on the order of 5 m s^{-1} in the central Pacific.

Figure 7 shows the 30-day mean geopotential-height field at 300 mb for the composite control run. Note that the results exhibit the characteristic features of a time-averaged Northern Hemisphere wintertime flow. In particular, the zonal asymmetries in the Northern Hemisphere height field indicate that the major midlatitude jets occupy their usual positions along the east coasts of Asia and North America. As expected, the east Asian jet is stronger and has greater longitudinal extent than the North American jet. The ridge along the west coast of North America is also reasonably positioned. In contrast with the Northern Hemisphere, the midlatitude height field in the Southern Hemisphere exhibits relatively little zonal asymmetry, owing to the lack of strong differential heating from land–sea temperature contrasts, especially during summer.

Figures 8a and 8b show the 30-day mean geopotential-height response at 300 and 700 mb, respectively. The magnitude of the response is comparable with those obtained by other investigators, although the present values may be slightly greater. Presumably, the response might be weaker if we average over many more cases. In general, the largest responses occur in the Northern Hemisphere. This is consistent with the findings of Simmons (1982) and Webster (1982), among others, who demonstrated that the remote response is usually strongest in the winter hemisphere and thus probably depends on properties of the mean winds in the subtropics.

The response over North America shows a familiar arcing pattern of alternating highs and lows. This pattern (including the response over Europe) is very similar to that obtained by Shukla and Wallace (1983), who examined the response of a climate model to the composite SST anomaly of Rasmusson and Carpenter (1982). The centers of the features in Fig. 8 are displaced downstream from those of the classical PNA teleconnection pattern described by Wallace and Gutzler (1981). In this case, the centers are located close to the nodes of the PNA pattern. Note that, in general, the largest responses occur in the vicinity of North America.

Figure 8 also shows that the midlatitude response has substantial equivalent barotropic structure, as indicated by the vertical phasing of the highs and lows and their increasing amplitude with height. This structure differs from that of the tropical response in Fig. 6, in which the large-scale flow is in opposite directions at upper and lower levels. The structure of the response in each region is consistent with the expected predominance of either shallow or deep vertical modes. This is examined in more detail in the remainder of this study.

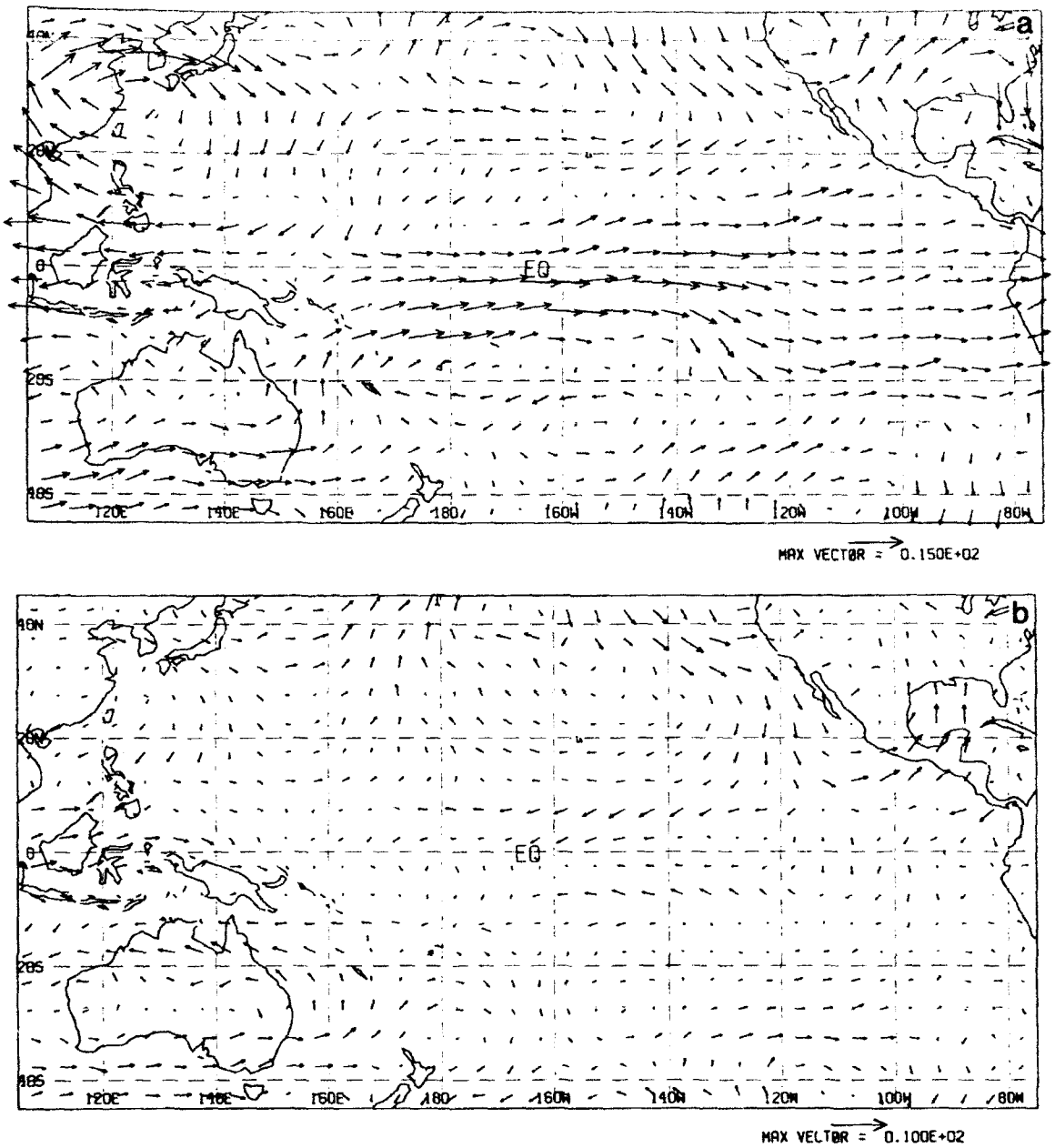

FIG. 6. The 30-day mean vector wind response over the Pacific at (a) 150 mb and (b) 925 mb. The maximum vector length corresponds to a wind speed of 15 m s^{-1} in (a) and 10 m s^{-1} in (b).

5. Normal-mode analysis

For practical purposes, we utilize the normal modes derived as part of the nonlinear normal-mode initialization (NNMI) scheme in the NOGAPS model. Accordingly, we should note that, while the use of a basic state at rest greatly simplifies the computation of the modes, it yields vertical structures that differ somewhat from those obtained with a more realistic (strong, vertically sheared) basic current. Therefore, care must be taken when attempting to interpret the physical processes that produce a particular modal response. The use of more realistic basic states in similar normal-mode decompositions has been considered by other

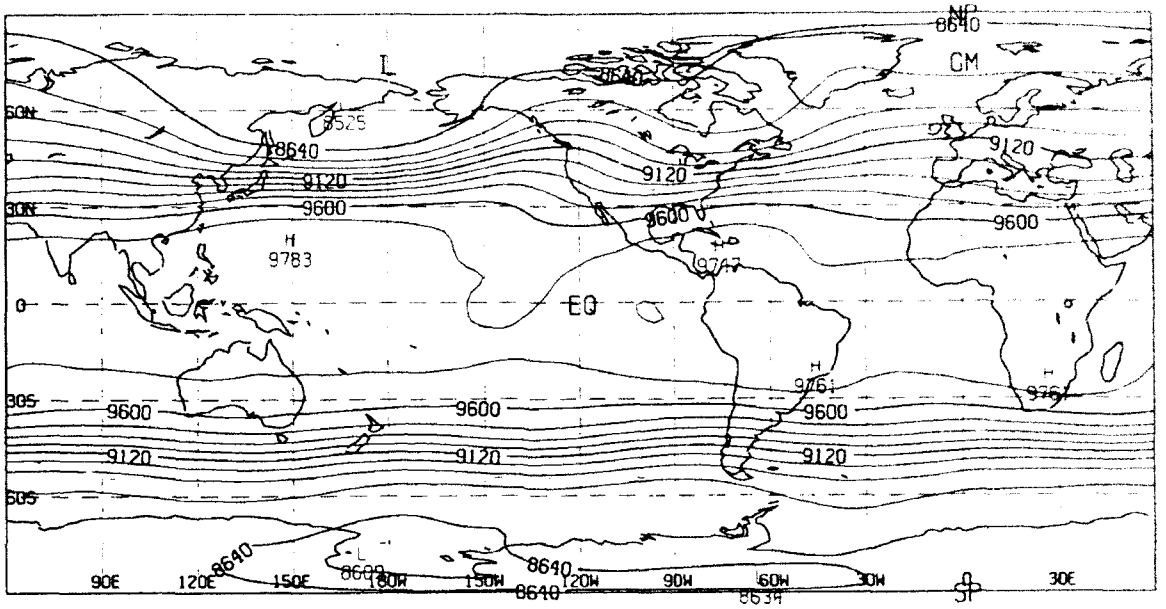

FIG. 7. The 30-day mean 300-mb geopotential-height field for the control run. The contour interval is 120 m.

investigators (Errico 1990, personal communication), but unfortunately, they are computationally impractical and are beyond the scope of this study.

a. Global energy

The structures of the modes have been normalized such that, for mode J, the total kinetic plus available potential energy E_J is given by the simple expression

$$E_J = \gamma \alpha_J \alpha_J^*, \tag{1}$$

in which α_J is the amplitude of mode J, γ is a constant that gives E_J dimensions of energy per mass, and an asterisk denotes a complex conjugate. The derivation of (1) is presented in the Appendix of GII. For now, it is of interest to note that if both the horizontal and vertical structure functions are orthogonal, then the modes contribute independently to the total energy E, and the quantity

$$\tilde{E} = \sum_J E_J \tag{2}$$

is equal to the total kinetic plus available potential energy of all the modes. The vertical modes of the NOGAPS model do not, in general, satisfy an appropriate orthogonality condition, and thus, $\tilde{E} \neq E$ in this study. It can be shown, however, that the vertical modes do satisfy this condition to a high degree for all but the shallowest equivalent depths so that $\tilde{E}$ is a close approximation to E (e.g., Errico 1989).

b. Time-varying response to forcing

To obtain the response energy for mode J, we replace (1) with

$$E_J^\delta = \gamma(\delta\alpha_J)(\delta\alpha_J^*), \tag{3}$$

where $\delta\alpha_J = (\alpha_J)_A - (\alpha_J)_C$ is the difference in the amplitude of mode J between the anomaly and control simulations. Note that E_J^δ is a positive-definite quantity not to be confused with the difference of the energy between the control and anomaly simulations. This is an appropriate diagnostic quantity in the present context because it represents a root-mean-square weighted average of the differences.

As an overview of the model response, Fig. 9 shows the total energy of the response (i.e., all mode types) as a function of vertical mode l for two 5-day means corresponding to days 1–5 and days 21–25 of the simulations. For each vertical mode l, we plot the quantity

$$E_l^\delta = \frac{1}{\tilde{E}^\delta} \sum_{J \in \mathcal{S}_l} E_J^\delta, \tag{4}$$

where the summation includes only modes that have equivalent depth h_l (denoted by the set $\mathcal{S}_l$), and $\tilde{E}^\delta$ is approximately equal to the total energy of the response defined analogously to (2).

For future reference, note that the set $\mathcal{S}_l$ does not necessarily include *all* modes with equivalent depth h_l except in those plots depicting the total (i.e., rotational plus gravitational) energy. The quantity E_l^δ thus rep-

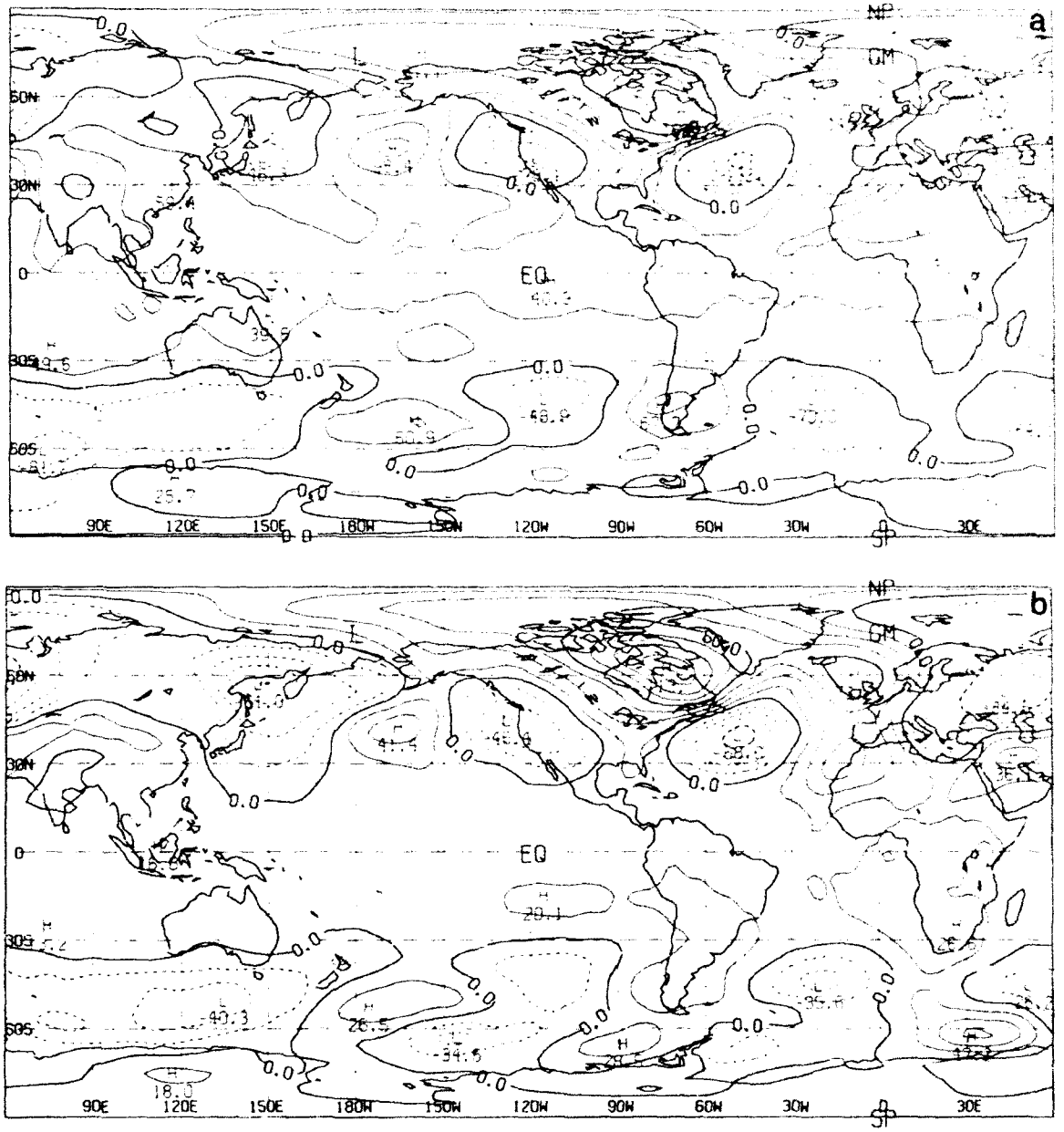

FIG. 8. The 30-day mean geopotential-height response at (a) 300 mb and (b) 700 mb. The contour interval is 30 m, with negative values denoted by dashed lines.

resents a normalized energy that describes the fractional contribution of a subset of modes to the total energy of the response. Also, the zonally symmetric modes have been excluded from these figures due to a formal problem in defining those modes corresponding to the mean velocity and geopotential fields (the former being zero valued in the linearized model). Although methods exist for treating these modes formally (Kasahara 1978; Errico 1987), their absence has little appreciable impact on the characteristics of the response; that is, there are only small differences between the zonal-mean states in the control and anomaly simulations.

Figure 9 shows the change in the total energy distribution among the vertical modes between days 1–5

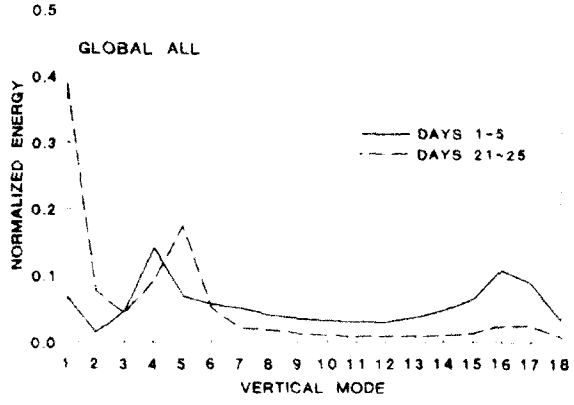

FIG. 9. The normalized total (all mode types) global response energy E_l^5 as a function of vertical mode l corresponding to days 1–5 (solid) and days 21–25 (dashed) of the simulations.

and days 21–25. During days 1–5, the internal modes dominate the response, particularly at $l = 4$, as well as at $l = 16$ and $l = 17$. By days 21–25, however, the external ($l = 1$) modes clearly dominate the response, contributing nearly 40% of the total energy. Only those modes corresponding to $l \leq 5$ contribute significantly to the response by this time, with the strongest medium-depth response shifting from $l = 4$ to $l = 5$.

The responses at $l = 16$ and $l = 17$ during days 1–5 may be due to direct thermal forcing by extremely shallow boundary-layer processes in response to the introduction of the SST anomaly. It should be cautioned, however, that the available potential energy measure that has been derived for the linearized model is not the same as for a nonlinear model (cf. Lorenz 1960b), and tends to exaggerate the significance of modes with very small equivalent depths (Errico 1987). In any case, these modes are of no physical interest in the present study.

A more detailed picture of the evolution of the response for vertical modes 1–5 is shown in Fig. 10. Here consecutive 5-day mean values of E_l^5 are plotted for each of these vertical modes. The energy contributions from all horizontal mode types is shown in Fig. 10a, while the contributions from the rotational and gravitational modes are shown separately in Figs. 10b and 10c, respectively. Note the different ordinate scaling for the gravitational modes in Fig. 10c.

Comparing Figs. 10a and 10b, we observe that the strong external mode response is comprised almost entirely of rotational modes, which is consistent with idealized modeling results suggesting that equivalent barotropic (and primarily nondivergent) Rossby waves play an important role in the response (Hoskins and Karoly 1981; Lim and Chang 1983; Webster 1981). This result is also consistent with the vertical phasing of the geopotential-height response shown in Fig. 8. Furthermore, the similarity of the growth curves after the first week in Figs. 10a and 10b indicates that the rotational modes clearly dominate the response at all vertical scales by this time.

The evolution of the $l = 4$ response in Fig. 10a is quite different—both qualitatively and quantitatively—from those of the other prominent responses at $l = 1$ and $l = 5$. The $l = 4$ response reaches its maximum value during days 1–5 and then rapidly approaches an approximate state of equilibrium. In contrast, the $l = 1$ and $l = 5$ responses reach their maximum values two to three weeks into the simulation. A comparison of Figs. 10b and 10c shows that the $l = 4$ response in Fig. 10a is primarily a gravitational-mode response initially. After days 6–10, however, the gravitational-mode energy at $l = 4$ decreases (Fig. 10c) while the rotational-mode energy at $l = 4$ increases toward its equilibrium value (Fig. 10b). The rapid peak in the gravitational-mode energy is undoubtedly due, in part, to the "shock" effect after the SST anomaly is introduced. In contrast, the responses at $l = 1$ and $l = 5$ are dominated by the rotational modes throughout most of their evolution.

The results suggest that the internal responses at $l = 4$ and $l = 5$ may be of different dynamical origins. Although the vertical structures of both modes are consistent with the "baroclinic" type of response associated with tropical convection, in which the large-scale flow reverses sign in the middle troposphere, the relatively slower growth of $l = 5$ and the predominance of the rotational modes throughout its evolution suggest that this may not necessarily be the case. Furthermore, we must consider that the nearly barotropic structure of the external mode in the troposphere (Fig. 1) is, by itself, inadequate for resolving the equivalent barotropic structure of the midlatitude response, which has increasing amplitude with height. Thus, the response at $l = 5$ (maximum amplitude at approximately 250 mb) may instead be another manifestation of the midlatitude response. This possibility is examined in further detail in GII, where the tropical modal response is separated from the midlatitude one.

The results in Fig. 10 demonstrate that a significant global response occurs rapidly, with all vertical modes shown obtaining (at least) a significant fraction of their final amplitudes in less than two weeks. An important implication of these results is that the time scale of the global response to tropical forcing is clearly relevant to deterministic NWP. In particular, the external rotational modes, which dominate the global response, contribute nearly 20% of the response energy after only approximately 1 week, and 30%–40% after 2–3 weeks. The medium-depth, internal rotational modes also play a major role, especially $l = 5$, which contributes 10% of the response energy after approximately one week and nearly 20% after two weeks.

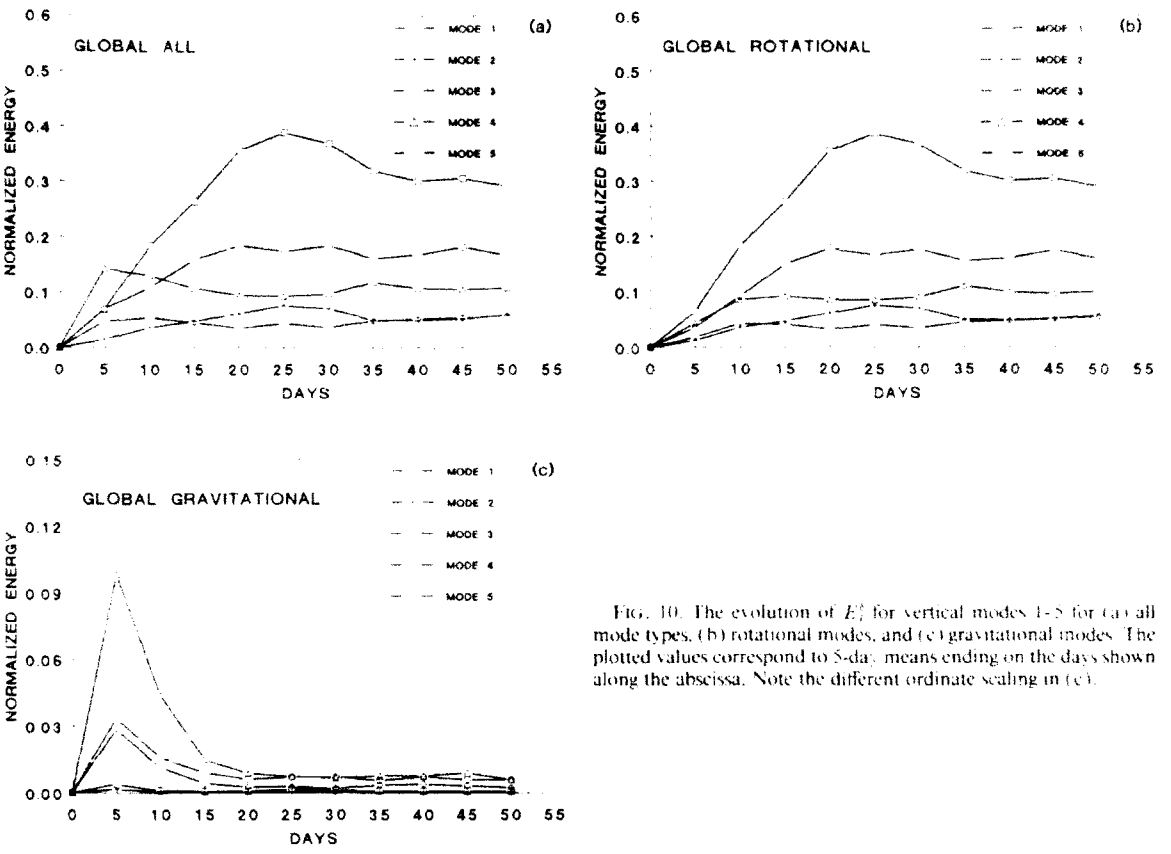

FIG. 10. The evolution of E_j^s for vertical modes 1–5 for (a) all mode types, (b) rotational modes, and (c) gravitational modes. The plotted values correspond to 5-day means ending on the days shown along the abscissa. Note the different ordinate scaling in (c).

6. Horizontal structure

Further insights into the mechanisms that produce global teleconnections may be gained by examining the dominant horizontal scales of the model response. Figure 11 shows the 30-day mean 300-mb streamfunction response, along with the contributions to the response from those modes corresponding to zonal wavenumbers 1–3 and 5–9. For convenience, these wave groups will be referred to as the long- and short-wave components of the response, respectively. Although there is evidence that other diagnostic approaches, particularly ones that account for two-dimensional wave dispersion, may be more appropriate than wavenumber separation for examining tropospheric variability (Wallace and Hsu 1983), the shortcomings of this technique are somewhat mitigated by focusing on wavenumber groups rather than individual wavenumbers.

Figures 11b and 11c reveal a dramatic difference between the response patterns at each scale. The long waves in Fig. 11b are zonally elongated and, in some locations, are aligned in patterns that suggest energy propagation from the tropics toward higher latitudes. The most prominent of these patterns originates in the far eastern equatorial Pacific near Ecuador and appears as a wave train that arcs northeastward along the east coast of the United States, and then toward southern Greenland. The amplitude and spatial scale of the waves increase with increasing latitude, consistent with simple theory. There are hints of a corresponding, but noticeably weaker, branch of the wave train in the Southern Hemisphere that arcs southeastward along the west coast of South America. This difference in amplitude is consistent with the results in Fig. 8, in which a generally weaker summer hemisphere response is shown.

The large longitudinal separation between the eastern Pacific wave train and the SST anomaly (Fig. 2) is striking and raises some concern as to whether this may be only a stochastic feature of a relatively small ensemble average. Webster and Chang (1988), however, have demonstrated that longitudinal trapping of equatorial wave energy can produce preferred, geographically fixed, regions along the equator for producing meridionally propagating responses. A conver-

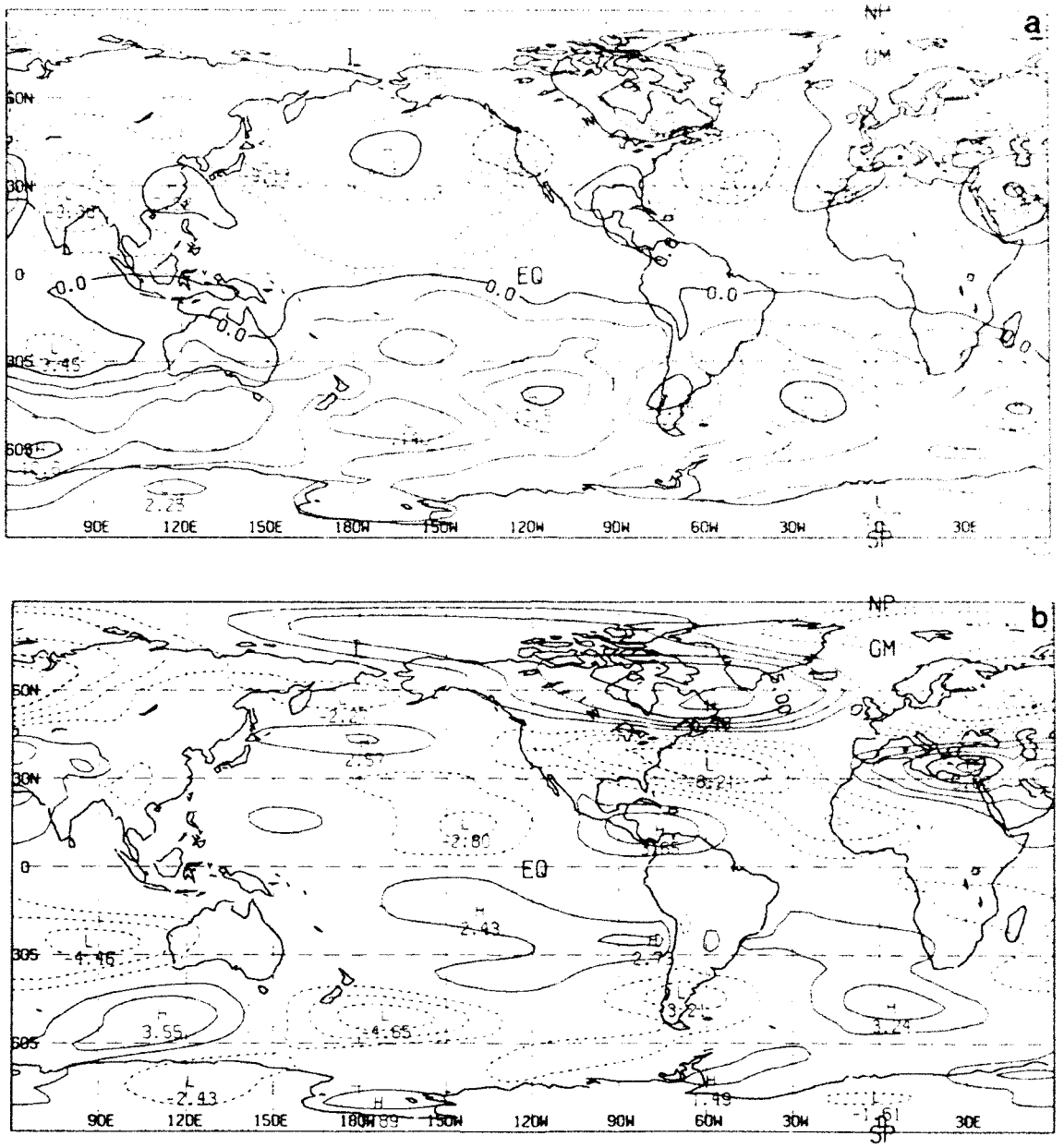

FIG. 11. The 30-day mean 300-mb streamfunction response for (a) all zonal wavenumbers, (b) wavenumbers 1–3, and (c) wavenumbers 5–9. The contour interval is 2.5×10^6 m^2 s^{-1} in (a) and 1.25×10^6 m^2 s^{-1} in (b) and (c), with negative values denoted by dashed lines.

gence of energy occurs in these locations due to differential changes in the group characteristics of tropical modes as they encounter zonal gradients in the background flow. These authors identified the eastern Pacific near 90°W—to the east of the westerly maximum in upper-tropospheric equatorial winds—as the primary location for the accumulation and subsequent meridional propagation of equatorial transient energy originating from as far away as the western Pacific. The location of the eastern Pacific wave train in Fig. 11b is generally consistent with this scenario, based on a preliminary analysis of the wind field. Moreover, in the

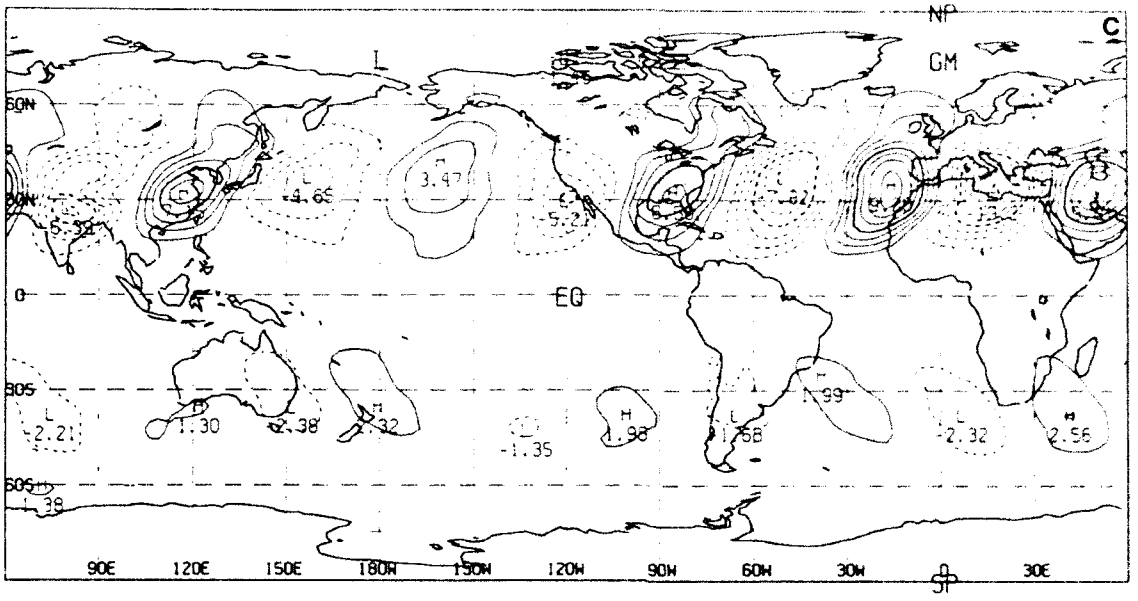

FIG. 11. (*Continued*)

present case there is also a substantial positive precipitation (heating) anomaly in the eastern-central equatorial Pacific near 145°W (Fig. 3b) that may be an effective energy source for this response. A more detailed analysis is required to confirm these speculations.

In the western Pacific, there is some indication that heating in the vicinity of the SST anomaly produces a meridionally propagating response in the Southern Hemisphere that emanates from just west of Indonesia and arcs along the west coast of Australia. In this case, the northern branch of the wave train is conspicuously absent.

In contrast to the long waves, the short waves in Fig. 11c are elongated meridionally rather than zonally and are aligned in a zonal pattern between latitudes 30° and 50° in both hemispheres. This component of the response bears a strong resemblance to the total response in Fig. 11a. In both hemispheres, there are zonal asymmetries in the magnitude of the response. In the Northern Hemisphere in particular, there is a pronounced increase in the magnitudes of the eddies as we move across the Atlantic. The response reaches its maximum amplitude over Europe where the eddies have more than twice the amplitude of those in the Pacific.

Figure 12 shows the evolution of the short-wave response at days 7, 9, and 10 of the simulation. At day 7 (Fig. 12a), the first organized pattern develops with eddies originating off the California coast and stretching across the United States and into the eastern Atlantic. The rest of the Northern Hemisphere is relatively undisturbed at this time. In the Southern Hemisphere, the eddies appear to originate in two locations: one in the eastern Pacific near 110°W, and the other in the extreme southwestern Indian Ocean. By day 9 (Fig. 12b), the response in the Northern Hemisphere has propagated eastward and equatorward into northern Africa. The eddies in the Northern Hemisphere continue to be strongest as they move into the Atlantic. In contrast, the response in the Southern Hemisphere attains its full longitudinal extent more rapidly due, at least in part, to the existence of the two apparent source points. By day 10 (Fig. 12c), the response in the Northern Hemisphere has spread across the Arabian peninsula and up into Asia, leaving only the eastern Pacific relatively undisturbed. The response develops on a time scale that is consistent with the ones observed in Fig. 10, which shows that the dominant modes grow rapidly during the first two weeks of the simulation.

Although the long- and short-wave partitionings used here are somewhat arbitrary, the results exhibit features that are consistent with some current theories of atmospheric teleconnections. In particular, they suggest that the background flow may play an important role in augmenting the extratropical response. This is especially compelling in the Northern Hemisphere, where the eddies develop near the exit region of the strong Pacific jet (cf. Fig. 7). Recently, Murphree et al. (1991) have shown that barotropically unstable regions on the equatorward flank of the subtropical or midlatitude jet

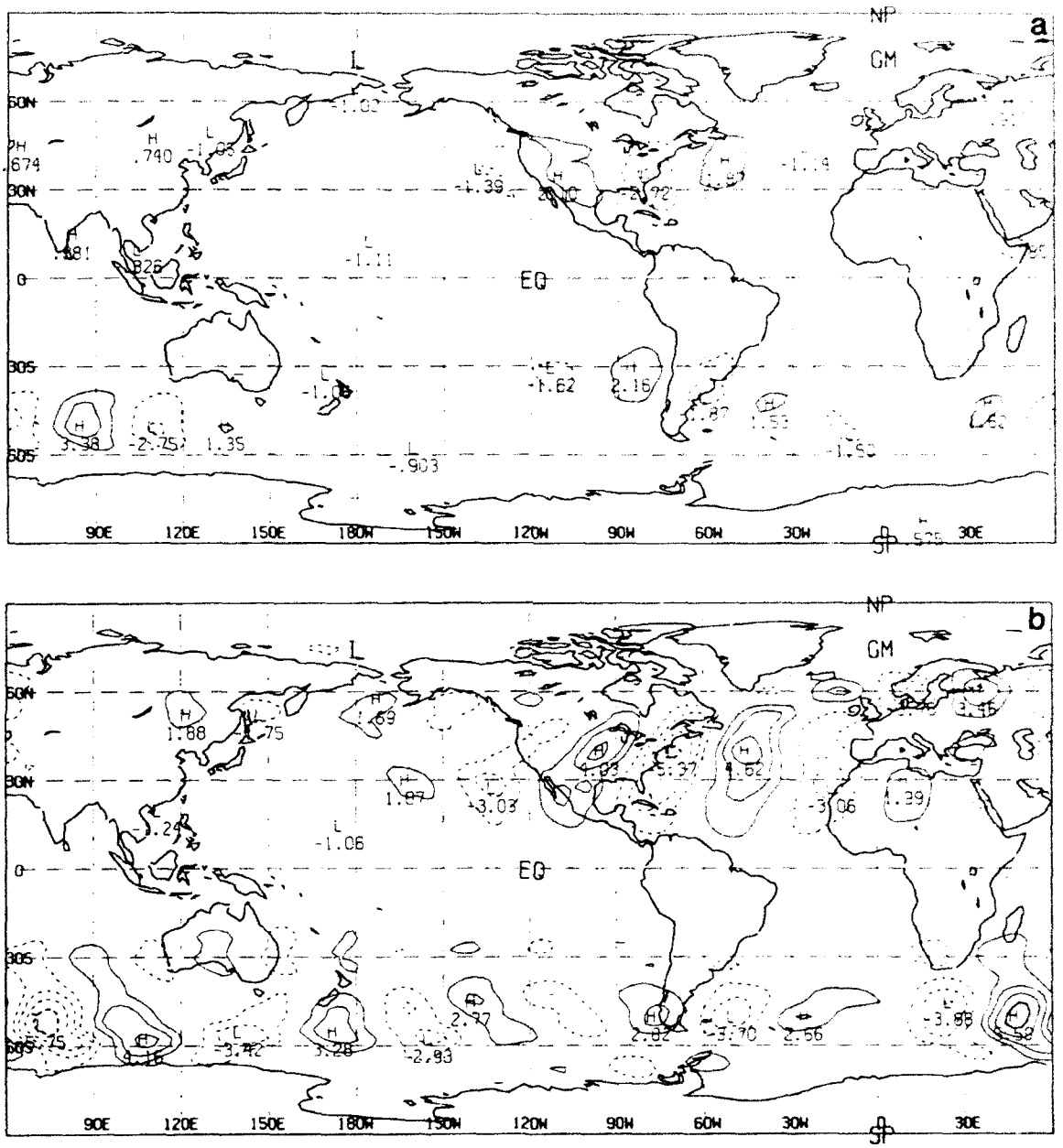

FIG. 12. The 300-mb streamfunction response for zonal wavenumbers 5–9 corresponding to (a) day 7, (b) day 9, and (c) day 10 of the simulations. The format is the same as in Fig. 11c.

can be the dominant energy source for producing an extratropical response to a tropical heating anomaly. Using the wave-energy flux vector developed by Plumb (1985), these authors showed that poleward-propagating energy from a tropical heat source may act primarily as a trigger mechanism for this instability, which, in turn, produces the type of wave response associated with midlatitude atmospheric teleconnections.

In the present case, it is also interesting to note that the eddies in Fig. 11c obtain local maxima just downstream from where the meridionally propagating re-

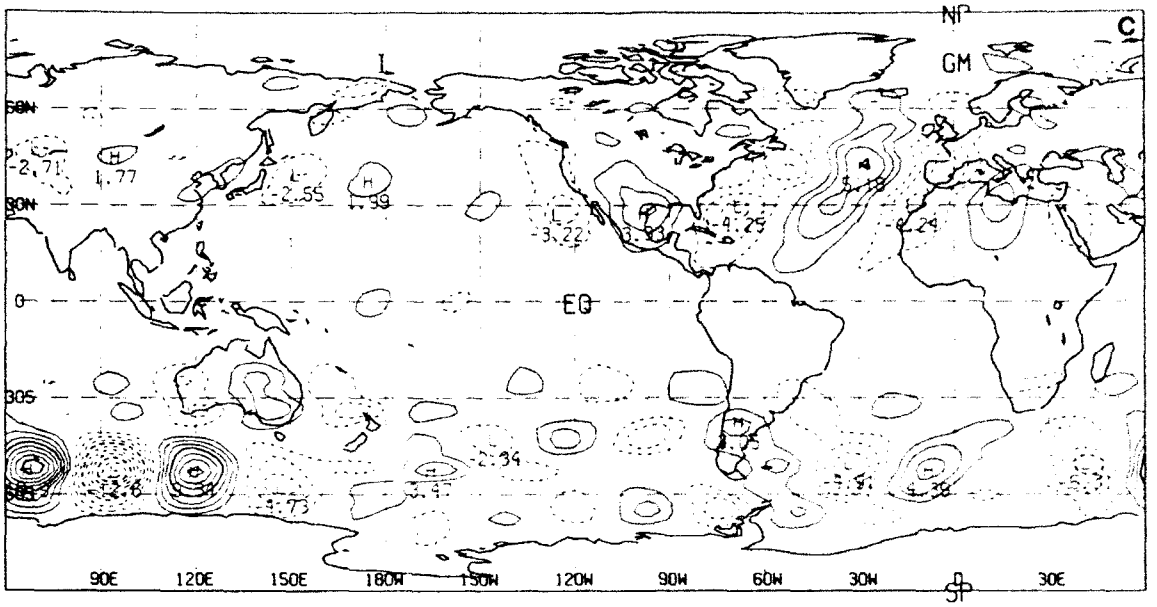

FIG. 12. (*Continued*)

sponses in Fig. 11b intersect the midlatitude westerly flow. Conversely, note that the absence of a local maximum in the North Pacific short-wave response is consistent with the absence of a northern branch of the meridionally propagating response emanating from Indonesia.

7. Conclusions

Rapid global-scale interactions between the tropics and extratropics were investigated by analyzing the response of the U.S. Navy's operational forecast model to localized SST anomalies in the tropical Pacific. The model normal modes were utilized, in addition to conventional difference-field diagnostics, to analyze the structure and evolution of the dominant horizontal and vertical modes of response. By monitoring the energy growth in these modes, it was shown that the qualitative and quantitative character of the long-term response is, to a large extent, well established after only one to two weeks of simulation. The results indicate that the global atmospheric response to tropical forcing can be rapid and may involve a series of dynamic mechanisms, especially in the extratropics.

The normal-mode analysis revealed that the external rotational modes dominated the global response after the first few days, with substantial secondary responses at vertical modes 4 and 5. Once equilibrium was established, the external modes accounted for over 30% of the response energy, while vertical modes 4 and 5 accounted for approximately 10% and 18%, respectively. The strong contribution from the external modes is consistent with the predominantly equivalent barotropic extratropical response, as demonstrated, for example, by the vertical structure of the 30-day mean geopotential-height response. It should be noted, however, that the external modes used in these calculations have predominantly barotropic (rather than equivalent barotropic) vertical structure because of the simple basic state used in their derivation. Thus, they are inadequate for describing phenomena that are strongly equivalent barotropic. This undoubtedly accounts for some portion of the response by the medium-depth internal rotational modes, which have their maximum amplitudes high in the troposphere. This conclusion is consistent with the growth rates for these modes being similar to those of the external modes, especially for vertical mode 5. In GII, a technique is presented for separating the tropical and extratropical modal responses in order to address some of these issues.

A decomposition of the extratropical response in terms of zonal wavenumber groups revealed two distinctly different types of wave patterns. The first type, which corresponded to wavenumbers 1–3, was characterized by zonally elongated waves aligned in patterns suggesting distinct regions of meridional energy propagation from the tropics toward higher latitudes. Interestingly, the most prominent of these patterns was separated longitudinally from the strongest tropical heating response. Certain aspects of these results are

consistent with the two-stage teleconnection scenario proposed by Webster and Chang (1988), in which transient tropical energy can propagate along the equator and become longitudinally trapped, thereby creating favorable emanation points for a meridionally propagating response.

The second type of wave pattern, which corresponded to wavenumbers 5–9 and bore a strong resemblance to the total response, gave further insights into mechanisms that may be important for producing the extratropical response. The growth rates of these waves were consistent with those of the dominant normal modes, but showed a wave pattern that developed in situ and propagated more or less zonally in the midlatitudes. The evolution of the pattern suggests that the background flow may play an important role in producing an extratropical response to tropical heating anomalies, as suggested by other investigators, including Simmons et al. (1983) and, more recently, Murphree et al. (1991).

The results reported here raise many questions that cannot be answered satisfactorily without further investigation. In particular, it would be useful to examine a larger number of cases in order to establish the robustness of features revealed by the wavenumber decomposition. Similarly, no attempt was made to examine the role of the mean winds in the tropics and subtropics in controlling the locations of the different wave responses, or their dependence on seasonal variations. A more rigorous investigation of how the extratropical response depends on interactions with the background flow is planned for future work. Also, the simple basic state used to derive the normal modes can be a complicating factor when trying to interpret how certain physical processes project onto the modes. The use of a more realistic basic state might simplify this problem, but would make computing the modes prohibitive.

Notwithstanding the above, these results clearly demonstrate the complexity of global-scale interactions resulting from tropical forcing and the rapid impact of these interactions on the general circulation over a broad range of spatial and temporal scales. With regard to NWP, the results imply that the prospect for extending our deterministic forecast capability beyond the medium range depends largely on our ability to eliminate, or at least slow the growth of, systematic errors in the tropics. This conclusion is similar to ones made by Tiedtke (1984) and Sardeshmukh and Hoskins (1988), who determined that uncertainties associated with present convective parameterization schemes may limit our prospects for making skillful long-range numerical forecasts. Finally, these results demonstrate the importance of developing new tools to diagnose the behavior of complex environmental models. This is the topic of Part II of this study (GII), in which we extend the normal-mode analysis presented here in order to investigate the structure and dynamics of the tropical and extratropical responses in more detail.

Acknowledgments. The author wishes to thank the reviewers for their helpful comments and suggestions for improving the manuscript. Special thanks are extended to Dr. T. Murphree of the Naval Postgraduate School and Dr. R. Errico of NCAR for their valuable discussions and comments on this work, and to Mr. S. Bishop for his help in preparing the figures.

Funding for this effort was provided by the Office of Naval Technology through the Predictive Systems Development Program (Program Element 62435N). Naval Research Laboratory Contribution 432:055:90.

REFERENCES

Arakawa, A., and W. Schubert, 1974: Interaction of a cumulus cloud ensemble with the large-scale environment: Part I. *J. Atmos. Sci.*, **31**, 674–701.

Barker, E. H., J. S. Goerss, and N. Baker, 1988: The Navy's operational multivariate optimum interpolation analysis method. Preprints, *Eighth Conf. on Numerical Weather Prediction*, Baltimore, Amer. Meteor. Soc., 161–163.

Bjerknes, J., 1969: Atmospheric teleconnections from the equatorial Pacific. *Mon. Wea. Rev.*, **97**, 163–172.

Blackmon, M. L., J. E. Geisler, and E. J. Pitcher, 1983: A general circulation study of January climate anomaly patterns associated with interannual variation of equatorial Pacific sea surface temperatures. *J. Atmos. Sci.*, **40**, 1410–1425.

Donner, L. J., H.-L. Kuo, and E. J. Pitcher, 1982: The significance of thermodynamic forcing by cumulus convection in a general circulation model. *J. Atmos. Sci.*, **39**, 2159–2181.

Errico, R. M., 1987: A description of software for determination of normal modes of the NCAR community climate model. NCAR Tech. Note, TN-277+STR, 86 pp. [NTIS PB89-113989.]

——, 1989: Theory and application of nonlinear normal mode initialization. NCAR Tech. Note, TN-344+IA, 137 pp.

Geisler, J. E., M. L. Blackmon, G. T. Bates, and S. Muñoz, 1985: Sensitivity of January climate response to the magnitude and position of equatorial Pacific sea surface temperature anomalies. *J. Atmos. Sci.*, **42**, 1037–1049.

Gelaro, R., 1992: A normal-mode analysis of rapid teleconnections in a numerical weather prediction model. Part II: Tropical and extratropical aspects. *Mon. Wea. Rev.*, **120**, 2914–2927.

Hogan, T. F., and T. Rosmond, 1991: The description of the Navy Operational Global Atmospheric Prediction System's spectral forecast model. *Mon. Wea. Rev.*, **119**, 1786–1815.

——, ——, and R. Gelaro, 1991: The NOGAPS forecast model: A technical description. NOARL Report 13, 212 pp. [NTIS AD-247 216.]

Horel, J. D., and J. M. Wallace, 1981: Planetary-scale atmospheric phenomena associated with the Southern Oscillation. *Mon. Wea. Rev.*, **109**, 813–829.

Hoskins, B. J., and D. J. Karoly, 1981: The steady linear response of a spherical atmosphere to thermal and orographic forcing. *J. Atmos. Sci.*, **38**, 1179–1196.

Julian, P. R., and R. M. Chervin, 1978: A study of the Southern Oscillation and Walker circulation phenomenon. *Mon. Wea. Rev.*, **106**, 1433–1451.

Kasahara, A., 1978: Further studies on a spectral model of the global barotropic primitive equations with Hough harmonic expansions. *J. Atmos. Sci.*, **35**, 2043–2051.

Keshavamurty, R. N., 1982: Response of the atmosphere to sea surface temperature anomalies over the equatorial Pacific and the teleconnections of the Southern Oscillation. *J. Atmos. Sci.*, **39**, 1241–1259.

Kok, C. J., and J. D. Opsteegh, 1985: Possible causes of anomalies in seasonal mean circulation patterns during the 1982–83 El Niño Event. *J. Atmos. Sci.*, **42**, 677–694.

Kwizak, M., and A. J. Robert, 1971: A semi-implicit scheme for grid point atmospheric models of the primitive equations. *Mon. Wea. Rev.*, **99**, 32–36.

Lim, H., and C.-P. Chang, 1983: Dynamics of teleconnections and Walker circulations forced by equatorial heating. *J. Atmos. Sci.*, **40**, 1897–1915.

Lord, S. J., W. C. Chao, and A. Arakawa, 1982: Interaction of a cumulus cloud with the large-scale environment. Part IV: The discrete model. *J. Atmos. Sci.*, **39**, 104–113.

Lorenz, E. N., 1960b: Energy and numerical weather prediction. *Tellus*, **12**, 364–373.

Louis, J.-F., 1979: A parametric model of vertical eddy fluxes in the atmosphere. *Bound.-Layer Meteor.*, **17**, 187–202.

Mechoso, C. R., A. Kitoh, S. Moorthi, and A. Arakawa, 1987: Numerical simulations of the atmospheric response to a sea surface temperature anomaly over the equatorial eastern Pacific Ocean. *Mon. Wea. Rev.*, **115**, 2936–2956.

Murphree, T., J.-M. Chen, P. Harr, and R. Gelaro, 1991: Short-term climate variations in the PNA region: The role of South Asian tropical west Pacific heating anomalies. Preprints, *Fifth Conf. on Climate Variations*, Denver, Amer. Meteor. Soc., 340–343.

Palmer, T. N., and D. A. Mansfield, 1986: A study of wintertime circulation anomalies during past El Niño events using a high resolution general circulation model. II: Variability of the seasonal mean response. *Quart. J. Roy. Meteor. Soc.*, **112**, 639–660.

Pitcher, E. J., M. L. Blackmon, G. T. Bates, and S. Muñoz, 1988: The effect of North Pacific sea surface temperature anomalies on the January climate of a general circulation model. *J. Atmos. Sci.*, **45**, 173–188.

Plumb, R. A., 1985: On three-dimensional propagation of stationary waves. *J. Atmos. Sci.*, **42**, 217–229.

Rasmusson, E., and T. Carpenter, 1982: Variations in tropical sea surface temperature and surface wind fields associated with the Southern Oscillation/El Niño. *Mon. Wea. Rev.*, **110**, 354–384.

Robert, A. J., 1966: The integration of a low order spectral form of the primitive meteorological equations. *J. Meteor. Soc. Japan*, Ser. 2, **44**, 237–245.

Sardeshmukh, P. D., and B. J. Hoskins, 1988: The generation of global rotational flow by steady idealized tropical divergence. *J. Atmos. Sci.*, **45**, 1228–1251.

Shukla, J., and J. M. Wallace, 1983: Numerical simulation of the atmospheric response to equatorial Pacific sea surface temperature anomalies. *J. Atmos. Sci.*, **40**, 1613–1630.

Simmons, A. J., 1982: The forcing of stationary wave motion by tropical diabatic heating. *Quart. J. Royal Meteor. Soc.*, **108**, 503–534.

——, J. M. Wallace, and G. W. Branstator, 1983: Barotropic wave propagation and instability, and atmospheric teleconnection patterns. *J. Atmos. Sci.*, **40**, 1363–1392.

Tiedtke, M., 1984: The effect of penetrative cumulus convection on the large-scale flow in a general circulation model. *Beitr. Phys. Atmos.*, **57**, 216–239.

Wallace, J. M., and D. S. Gutzler, 1981: Teleconnections in the geopotential height field during the Northern Hemisphere winter. *Mon. Wea. Rev.*, **109**, 785–812.

——, and H.-H. Hsu, 1983: Ultra-long waves and two-dimensional Rossby waves. *J. Atmos. Sci.*, **40**, 2211–2219.

Webster, P. J., 1981: Mechanisms determining the atmospheric response to sea surface temperature anomalies. *J. Atmos. Sci.*, **38**, 554–571.

——, 1982: Seasonality in the local and remote atmospheric response to sea surface temperature anomalies. *J. Atmos. Sci.*, **39**, 41–52.

——, and H.-R. Chang, 1988: Equatorial energy accumulation and emanation regions: Impacts of a zonally varying basic state. *J. Atmos. Sci.*, **45**, 803–829.